

THESIS FOR THE DEGREE OF LICENTIATE OF PHILOSOPHY

Protons in In-doped BaZrO₃:
incorporation, distribution and local environments

LAURA MAZZEI



CHALMERS

Department of Physics

CHALMERS UNIVERSITY OF TECHNOLOGY

Gothenburg, Sweden 2016

**Protons in In-doped BaZrO₃:
incorporation, distribution and local environments**
LAURA MAZZEI

©LAURA MAZZEI, 2016

Department of Physics
Chalmers University of Technology
SE-412 96 Göteborg, Sweden

Typeset in L^AT_EX. Figures created using IGOR and Adobe Illustrator CC 2015.

Chalmers Reproservice
Göteborg, Sweden 2016

Protons in In-doped BaZrO₃:
incorporation, distribution and local environments

Laura Mazzei
Department of Physics
Chalmers University of Technology

Abstract

Acceptor doped proton conducting oxides are currently of large interest for their potential application as electrolyte materials in the future generation of solid oxide fuel cells. However, their proton conductivities are still lower than the target conductivity required for practical applications. The development of new materials with better performance depends on the advance of our understanding of the atomic-scale structure and dynamics, and their coupling with macroscopic proton conductivity, in the currently available materials. The aim of this thesis is to obtain new insights into the structure and dynamics in In-doped BaZrO₃, one of the most investigated and promising classes of proton conducting oxides. To achieve this aim, the thesis is divided into two, complementary, research themes. The first research theme is dedicated to the analysis of the O-H vibrational spectra and a detailed characterization of the different proton sites present. Of specific interest is the nature of the hydrogen bond between the protons and neighboring oxygen atoms, O-H···O, which relates to the proton conducting properties. The second research theme focuses on studies of the proton concentration depth profile and proton conductivity in thin films of the same material. The investigations were performed using a combination of inelastic neutron scattering, infrared spectroscopy, molecular dynamics simulations, X-ray diffraction, Rutherford backscattering, X-ray and neutron reflectivity, nuclear reaction analysis and impedance spectroscopy. The results show that for low In-doping levels the protons are predominantly found close to the dopant atoms. These proton sites are characterized by a relatively weak hydrogen bonding and act as traps for the protons. For higher In-doping levels the results reveal the presence of a growing population of proton sites associated with stronger hydrogen bonds, and the trapping effect around the dopant atoms is now less pronounced, or even removed. In the studies of thin film samples, a key result is the observation of the presence of a thin proton-enriched near-surface region, characterized by relatively weak hydrogen bonding and lower proton mobility compared to the bulk of the material.

Keywords: *Proton conductors, perovskites, thin films, hydrogen dynamics, vibrational spectroscopy, neutron scattering, hydrogen depth profiling.*

LIST OF PUBLICATIONS

This thesis is based on the following publications:

I Structure and proton vibrational dynamics of the proton conducting perovskite $\text{BaZr}_{0.9}\text{In}_{0.1}\text{O}_3\text{H}_{0.1}$

A. Perrichon, L. Mazzei, G. Wahnström, S. F. Parker, L. Börjesson, M. Karlsson.

In manuscript

II Vibrational Spectra of the Proton Conducting Perovskite

$\text{BaZr}_{0.5}\text{In}_{0.5}\text{O}_3\text{H}_{0.5}$

L. Mazzei, A. Perrichon, A. Mancini, S. F. Parker, L. Börjesson, L. Malavasi, M. Karlsson.

In manuscript

III Structure and Conductivity of Epitaxial Thin Films of In-doped BaZrO_3 Based Proton Conductors

L. Mazzei, M. Wolff, D. Pergolesi, J. A. Dura, L. Börjesson, P. Gutfreund, M. Bettinelli, T. Lippert, and M. Karlsson

Submitted

Additional publications not included in this thesis

IV Structure and dehydration mechanism of the proton conducting oxide $\text{Ba}_2\text{In}_2\text{O}_5(\text{H}_2\text{O})_x$

J. Bielecki, S. F. Parker, L. Mazzei, L. Börjesson, M. Karlsson

Journal of Materials Chemistry A **4**, 1224-1232 (2016)

THE AUTHOR'S CONTRIBUTION TO THE PAPERS

- I I contributed to the samples' preparation and characterization, performed the INS experiments and data analysis and was the leading author of the corresponding parts of the paper. I contributed to the interpretation of the results and to the writing of the paper.
- II I contributed to the samples' characterization and preparation. I performed the INS and IR experiments and data analysis. I was the main author of the paper.
- III I contributed to the samples' characterization and preparation. I contributed to the IS, NRA and XRR experiments and data analysis and performed the NR experiments and data analysis. I was the main author of the paper.

Contents

Glossary	1
Introduction	2
1 BaZrO₃ based proton conductors	5
1.1 Proton conducting perovskite oxides for SOFC applications . . .	5
1.2 Acceptor doped perovskites	6
1.3 Proton dynamics	9
1.3.1 The role of the structure on the proton dynamics	11
2 Methods	15
2.1 Vibrational spectroscopy	15
2.1.1 Infrared spectroscopy	16
2.2 Inelastic neutron scattering	16
2.3 X-ray and neutron reflectivity	20
2.4 Nuclear reaction analysis	24
3 Instrumentation	27
3.1 The MERLIN and TOSCA spectrometers	27
3.2 IR spectrometers	29
3.3 Neutron reflectometers	30
4 Summary of results	33
4.1 Paper I	33
4.2 Paper II	34
4.3 Paper III	34
5 Conclusions and Outlook	37
Acknowledgments	39

Bibliography	40
Paper I-III	49

Glossary

<i>eSDL</i>	Electronic scattering length density
INS	Inelastic neutron scattering
IR	Infrared
IS	Impedance spectroscopy
IT	Intermediate temperature
NR	Neutron reflectivity
NRA	Nuclear reaction analysis
<i>nSLD</i>	Neutron scattering length density
RBS	Rutherford backscattering
<i>SLD</i>	Scattering length density
SOFC	Solid oxide fuel cell
TOF	Time of flight
XRR	X-ray reflectivity
<i>M</i> :BZO	<i>M</i> doped BaZrO ₃
50In:BZO	BaZr _{0.5} In _{0.5} O ₃ H _{0.5}
10In:BZO	BaZr _{0.9} In _{0.1} O ₃ H _{0.1}

Introduction

Proton conducting oxides are an important class of materials which have attracted considerable interest in relation to a wide range of technological applications, in particular through their usage as electrolytic membranes in solid oxide fuel-cell (SOFC) technology [1–3]. One of the major challenges for the SOFC technology is the development of devices operating in the intermediate temperature (IT) range (200–500 °C) and, in this respect, solid oxides with the perovskite structure show the greatest promise [4–8]. However, the proton conductivities of present-day proton conducting perovskites are still below the target conductivity ($\approx 10^{-2} \text{ Scm}^{-1}$) required for their practical use. Hence, before IT-SOFC technology is likely to be a viable method of power generation, more highly conductive proton conducting oxides need to be developed [4, 6].

The development of new perovskite oxides which match the criteria for technological applications depends on developing a better understanding of the physicochemical factors limiting the proton conductivity in those materials that are already available. This requires a deeper knowledge of the coupling between proton conductivity and atomic scale structure and dynamics, characterized by, *e.g.*, the chemical composition, the short- and long-range structure, structural defects, impurities and structural distortions in the perovskite material. Considering, as an example, acceptor doped BaZrO_3 based oxides, it has been observed that the IT conductivity varies considerably depending on the choice of the type of dopant [9, 10], *e.g.* between 10^{-5} and 10^{-2} Scm^{-1} at $T = 300 \text{ °C}$, yet the reason for this spread of the proton conductivity is not fully understood [11–16]. Further, for certain applications, such as miniaturized SOFCs, one would use thin film electrolytes ($\lesssim 1 \mu\text{m}$) sandwiched between the anode and cathode [2, 17–19]. Differently from powder samples, such films represent a confined state and furthermore can be textured, strained, and exhibit varying degrees of crystallinity, which may affect significantly the performance of the electrolyte [20–23]. In this context, it is important to extend the understanding of the structure and coordination of protons in bulk powder samples to thin films.

To take on some of these challenges, this thesis focuses on studies of the local structural properties in proton conducting perovskites, both bulk and thin films, and is divided into two, complementary themes. The first theme concerns the study of the local environments of protons in $\text{BaZr}_{0.9}\text{In}_{0.1}\text{O}_3\text{H}_{0.1}$ (10In:BZO) and $\text{BaZr}_{0.5}\text{In}_{0.5}\text{O}_3\text{H}_{0.5}$ (50In:BZO). In particular, the study focuses on the investigation of the role of local environments on vibrational modes and proton dynamics. The second theme concerns the study of the incorporation and distribution of protons in epitaxial thin films of 50In:BZO. The work pays particular attention to the connection between the structural properties of the perovskite structure, proton concentration and conductivity. Thin films are particularly suitable for this kind of investigation, since well-established depth profiling techniques, as for instance reflectivity and nuclear reaction analysis, can be used. The choice of system, *i.e.* In-doped BaZrO_3 (In:BZO), combines a relatively simple average structure (cubic) with a high nominal concentration of protons after hydration, thus providing a good signal/contrast in the experiments. Moreover, In:BZO has been widely investigated in the past [10–12, 16, 24–34], which provides important background knowledge, necessary to discuss the implications of the results obtained.

The thesis is organized as follows. Chapter 1 provides a general background knowledge about proton conducting oxides, with a focus on the structural and dynamical properties of acceptor doped BaZrO_3 . Chapter 2 provides a description of the main experimental methods used in this thesis, while Chapter 3 gives details on the specific instrumentation that has been used for the studies. Chapter 4 and Chapter 5 provide a summary of the obtained results and an outlook for future works in the field.

Chapter 1

BaZrO₃ based proton conductors

1.1 Proton conducting perovskite oxides for SOFC applications

SOFCs are, as mentioned before, the intended target application for the materials investigated in this thesis [5]. SOFCs¹ are commonly based on oxide ion conducting electrolytes with an operation temperature above 800 °C [36]. Expanding the operation temperature window towards lower temperatures would imply several advantages in terms of durability and cost of the components and in terms of start-up time of the devices, which currently are the major drawbacks of SOFCs based on oxide ion conductors. In this context, proton conducting electrolytes, especially materials based on the fluorite, perovskite and apatite structures [6, 7, 19], are among the most promising candidates to lower the operating temperature of SOFCs towards the IT range (200–500 °C).

Of specific concern of this thesis are proton conductors based on acceptor doped perovskite oxides. Between the 1980 and 1990 Iwahara and coworkers reported for the first time the possibility to conduct protons through these oxides and suggested to use acceptor doped SrCeO₃, BaCeO₃ and BaZrO₃ as proton conducting materials [9, 38–41]. Since then, the chemical, thermal and transport properties of several compounds have been investigated. Among others, BaZrO₃ based proton conductors have drawn considerable attention due to their ability to combine chemical stability with high proton conductivity

¹A description of the working principle of SOFCs, their electrolytes and properties can be found elsewhere [2, 4, 6, 19, 35–37].

in the IT range, where they reach values up to 10^{-3} – 10^{-2} S·cm $^{-1}$ [4, 6, 42, 43]. A brief description about the general properties of these materials is given in the following.

1.2 Acceptor doped perovskites

Perovskite type oxides are compounds with the general formula ABO_3 , where A usually is a large divalent cation, such as Ba^{2+} or Sr^{2+} , and B usually is a smaller tetravalent ion, as for instance Zr^{4+} . The ideal perovskite structure exhibits a cubic unit cell for which the A cations occupy the body centered positions and the BO_6 octahedra occupy the corners of a cube, as schematically illustrated in Figure 1.1(left). Deviations from this “ideal” structure are observed when the sizes of the cations are incompatible with the sizes of the respective interstitial positions. This incompatibility may be quantified by the *Goldschmidt tolerance factor*, $t_G = (R_A + R_O)/\sqrt{2}(R_B + R_O)$, where R_A , R_B , R_O are the respective atomic radii of the A , B and O ions. For an ideal cubic perovskite, $t_G = 1$ [44, 45]. $BaZrO_3$ is an example of a nearly perfect cubic perovskite structure, with $t_G = 1.01$ [45], belonging to the symmetry space group $Pm\bar{3}m$ [6, 46–50].

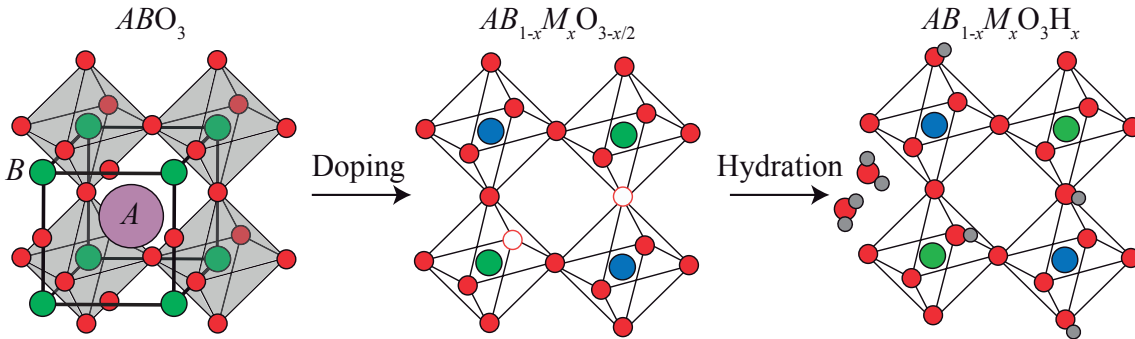
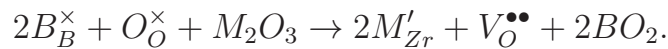


Figure 1.1: Schematic illustration of the cubic perovskite structure, acceptor doping and hydration.

Since protons are not inherently part of the perovskite structure, they need to be introduced into it in some way. This can be achieved by the formation of oxygen vacancies and the subsequent reaction between oxygen vacancies and water vapor. An oxygen deficient structure, $AB_{1-x}M_xO_{3-x/2}$, can be obtained by acceptor doping, which consists in the substitution of some of the B^{4+}

cations with cations of lower valency, *e.g.* M^{3+} . In Kröger-Vink notation² this may be expressed as



The reaction between oxygen vacancies and water vapour, referred to as hydration, protonation or proton loading, leads to the formation of hydroxyl ions on oxygen sites, *i.e.*



Hydration may be achieved by exposing the material to a humid atmosphere during heating. The water molecules dissociate on the surface of the sample into hydroxyl groups (OH^-), which fill the oxygen vacancies, and protons, which bind to lattice oxygens. The protons diffuse towards the bulk of the material, and, at the same time, oxygen vacancies diffuse towards the surface. In this way, more and more water molecules can dissociate on the surface of the sample and this leads, under the assumption that all oxygen vacancies are filled, to a fully hydrated structure, $AB_{1-x}M_xOH_x$.

Assuming an ideal behavior, the concentration of hydroxyl ions at the equilibrium condition can be expressed as³

$$[OH_O^\bullet]_T = 3 \frac{p_w K(T)}{p_w K(T) - 4} \left[1 - \sqrt{1 - \frac{p_w K(T) - 4}{p_w K(T)} \left(\frac{2[A]}{3} + \frac{2[A]^2}{9} \right)} \right], \quad (1.2)$$

where $K(T)$ is the equilibrium constant as a function of the temperature T , given by

$$K(T) = e^{\left(-\frac{\Delta H^0 - T\Delta S^0}{k_b T} \right)}. \quad (1.3)$$

Here the notation $[\]$ stands for concentration, p_w is the water partial pressure and ΔH^0 and ΔS^0 are the hydration enthalpy and entropy, respectively.

Figure 1.2 shows the concentration of hydroxyl ions for 50In:BZO as calculated using Eq.(1.2) at conditions relevant for the work in this thesis. As

²In Kröger-Vink notation, M_B indicates an atom M on a B site and V_B indicates a vacancy on a B site. The symbols \times , \bullet and $'$ represent neutral, negative and positive charges, respectively.

³In this derivation the following equations have been used

$$K(T) = \frac{[OH_O^\bullet]^2}{[V_O^{\bullet\bullet}][O_O^\times]p_w}, \quad [OH_O^\bullet] + 2[V_O^{\bullet\bullet}] - [M] = 0, \quad [OH_O^\bullet] + [V_O^{\bullet\bullet}] + [O_O^\times] = N_O \equiv 3,$$

expressing the equilibrium constant of the reaction in Eq.(1.1), the charge neutrality condition and the site restriction for the oxygen site, respectively [42, 51].

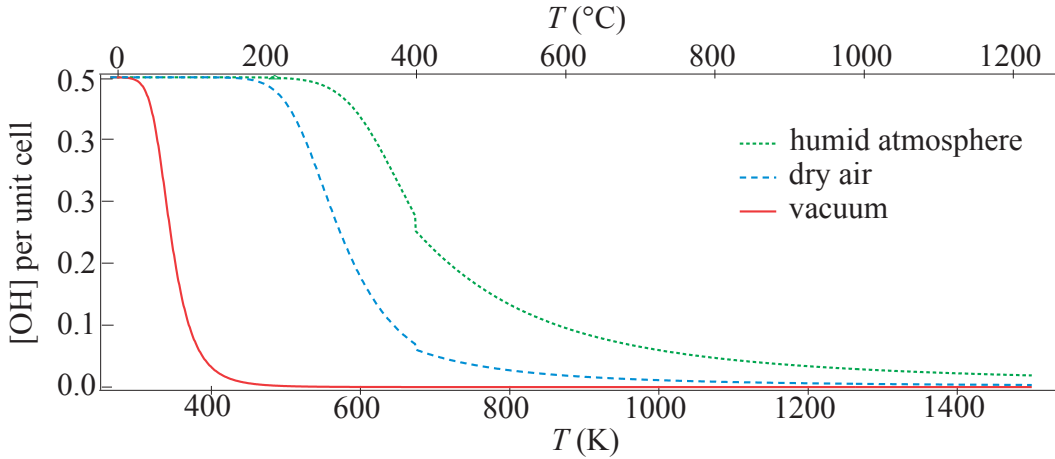


Figure 1.2: Theoretical concentration of OH_{\bullet} in 50In:BZO as a function of temperature in a humid atmosphere ($p_w = 0.46$ bar), dry air ($p_w = 0.0126$ bar), and vacuum ($p_w = 10^{-8}$ bar), respectively, calculated using the values for the hydration enthalpy and entropy as provided in Ref. [31].

it can be seen, a complete hydration ($[OH_{\bullet}] = [A]$) can be achieved only in a certain range of temperatures and partial pressures. It is important to notice that Eq.(1.2) does not provide information on the time necessary to reach the equilibrium condition. This time decreases as the temperature increases, since the mobility of both protons and oxygen vacancies increases with temperature [7, 42]. Therefore, one would like to use a quite high hydration temperature to enhance the mobility, but a quite low hydration temperature to assure a full hydration. Generally, a good compromise is to perform the hydration at intermediate temperature [200–400 °C] and elevated water pressure by using a humid atmosphere, *cf.* the green curve in Figure 1.2.

Interestingly, the protonation degree achieved by hydrating acceptor doped $BaZrO_3$ materials varies in a quite broad range, between 60% and 100% [10, 14, 25, 31, 42, 52–55], and, in a few reported cases, even hydration degrees higher than 100% have been observed [16, 55]. The presence of unfilled oxygen vacancies or an excess of protons leads to the formation of a variety of different proton sites, as it will be discussed in the next section, and, furthermore, this fact points towards the likelihood of an uneven distribution of protons in the material. The effect of such an uneven distribution of protons on the material's proton conductivity is not known, but rather it is one of the key questions of this thesis.

1.3 Proton dynamics

Once a proton is introduced in the acceptor doped perovskite, it can be considered as a protonic defect in a host structure, relatively free to move. The proton dynamics may be divided into long-scale phenomena, such as conduction and long-range diffusion, and short-range phenomena, such as elementary transport steps and local dynamical processes. The conductivity, $\sigma(T)$, is related to the proton diffusion coefficient, D_σ , through the Nernst-Einstein equation

$$D_\sigma = \sigma(T) \frac{k_B T}{e^2 N},$$

where k_B is the Boltzmann constant, e the proton charge and N the number density of the mobile protons. While the conductivity depends on the available number of charge carriers (protons), the diffusion coefficient directly reflects the ability of the protons to diffuse in the material.

Turning now to the atomic scale, the protons, in addition to the covalent O-H bonds, usually form hydrogen bonds with the neighboring oxygen atoms, thus occupying a double-Morse type potential [Figure 1.3]. The orientation and length of both bonds, together with the potential barrier, are strongly influenced by the environment around the protons [24, 27, 30, 56]. It should be noted that the presence of several different local environments is a direct consequence of the presence of dopant atoms and unfilled oxygen vacancies, which can be seen as local defects in the oxide's structure [Figure 1.4]. Furthermore, different environments can be characterized by different local distortions of the lattice. It is widely accepted that the transport of protons occurs through the so-called Grotthuss mechanism [8, 42], *i.e.* the repetition of two elementary steps: i) transfer of the protons between oxygen atoms and ii) reorientation of the O-H bonds. As illustrated in Figure 1.5(a), a proton can be transferred from an oxygen O(1) to a neighbouring oxygen O(2). The transition from the initial state O(1)-H··O(2) to the final state O(1)··H-O(2) requires the overcome of the energy barrier between the two proton sites. Eventually, the O(1)··H bond can be broken and the H-O(2) bond is free to rotate until a new hydrogen bond, to any other oxygen of the perovskite lattice, is created [Figure 1.5(b)]. A sequence of these elementary steps leads to long-range diffusion [8, 42].

Protons also participate to the O-H vibrational modes, bend (also referred to as wag or libration) and stretch, which are schematically illustrated in Figure 1.5(c)-(d). O-H stretch and bend modes are referred to as local vibrational modes since, unlike phonons, they do not propagate throughout the lattice. It

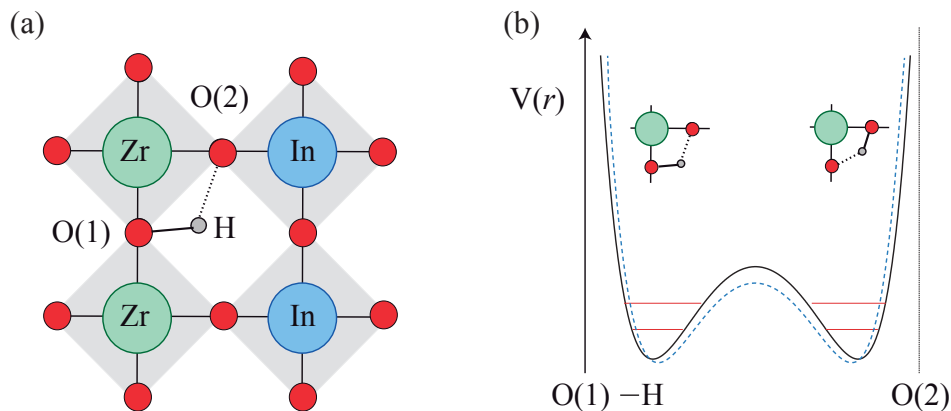


Figure 1.3: (a) Schematic illustration of a proton site in In:BZO and (b) of the double-Morse type potential, $V(r)$, as described in the text. The blue line indicates a change in the potential shape due to changes in the O(1)-O(2) separation distance. Red lines indicate the vibrational ground and first excited states of the O-H stretch mode.

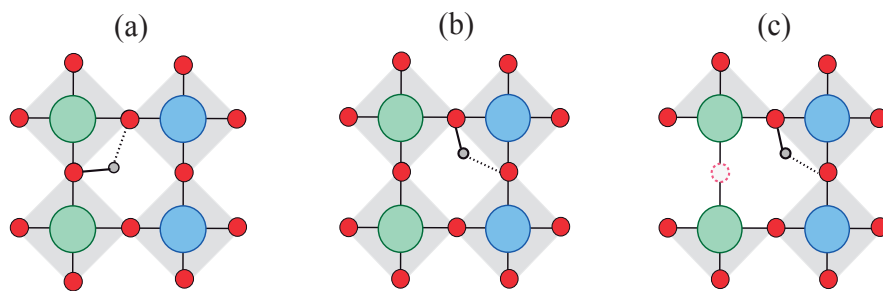


Figure 1.4: Examples of local proton environments in In:BZO where the proton site is located (a) between two Zr atoms, (b) between one Zr and one In and (c) close to an oxygen vacancy.

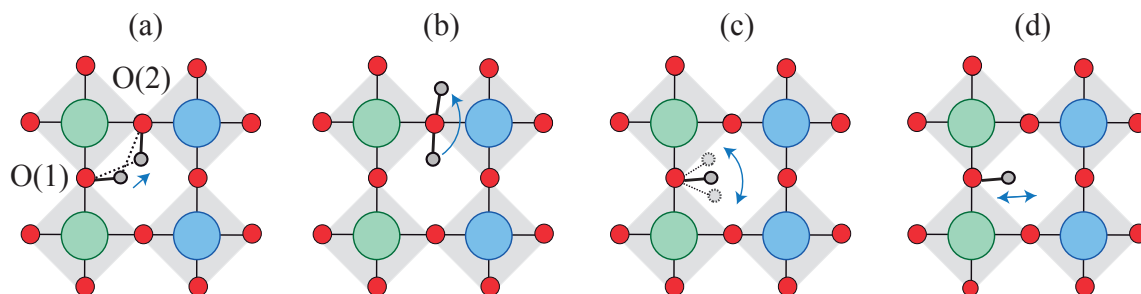


Figure 1.5: Schematic 2-D representations of (a) a proton transfer, (b) a O-H bond reorientation, (c) O-H bend mode and (d) O-H stretch mode.

has been suggested that the O-H vibrational dynamics are closely related to the proton transport and that both the transfer step and the reorientation step can be promoted by thermal or optical excitation. For instance, if the first O-H stretch vibrational level is populated, the energy barrier between the two minima of the double-Morse type potential is effectively lowered [Figure 1.3], thus vibrational dynamics may promote the transfer step [8, 24, 57, 58]. The role of the O-H local dynamics in the transport process has been investigated in previous works by Sphar *et al.* [57, 58] using a picosecond transient bleaching technique combined with high-resolution infrared (IR) absorption spectroscopy. Their analysis of hydrogen local dynamics in Rutile TiO₂ showed that when a stretch mode is excited, it couples with a bend mode which promotes the transfer process. Therefore, it is likely that stretch and bend modes play crucial roles in the proton diffusion process also in acceptor doped BaZrO₃. It is important to notice that in TiO₂ the O-H stretch band is a sharp peak at 407 meV, whereas acceptor doped perovskite-like oxides are characterized by very broad bands, which relate to the presence of hydrogen bonds and different proton sites [28, 32, 42, 52]. Regarding the materials of concern of this thesis, In:BZO, the O-H stretch modes are found at energies between 250 and 450 meV, whereas the O-H bend modes are characterized by energies between 100–150 meV.⁴ Previous work suggests that the dominant feature in the O-H stretch region (320–450 meV, see Figure 1.6) is the result of several O-H stretch bands, each one related with a specific proton site and characterised by a different degree of hydrogen bonding. In particular, proton sites where the protons are strongly hydrogen-bonded result in a shift of the O-H stretch modes towards lower energies (red-shift) [24]. The presence of different proton sites (and different degrees of hydrogen bonding) may result in the presence of different rates of proton transfer and bond reorientation, depending on the specific site.

1.3.1 The role of the structure on the proton dynamics

As previously mentioned, the proton dynamics (vibrational dynamics, elementary transport steps and long-range diffusion) are influenced by the presence of the dopant atoms. As an example, in acceptor doped BaZrO₃ the maximum proton conductivity at a specific temperature can vary several orders of magnitude, *i.e.* from 10^{-5} to 10^{-2} Scm⁻¹ at $T = 300$ °C, depending on the nature of the trivalent dopant, *e.g.* Ga, Sc, In, Gd or Y, where Y:BZO is the

⁴Reports on experimental and calculated O-H vibrational frequencies in acceptor doped perovskite oxides can be found elsewhere [24, 28, 32, 34, 42, 52, 56, 59].

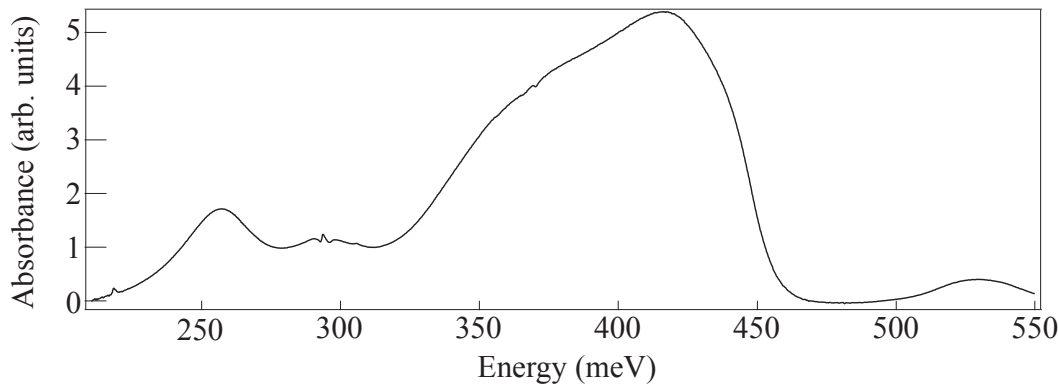


Figure 1.6: IR absorbance spectra over the O-H stretch region of hydrated 50In:BZO [see Paper II].

material showing the highest proton conductivity, and Ga:BaZrO₃ is the one showing the lowest [9, 10, 14, 15]. Furthermore, it has been shown that the increase of the doping level may hinder the diffusion of the protons in acceptor doped BaZrO₃ [31, 55]. Concerning the nature of the dopant atoms, some studies suggest a strong relation between the ionic radii of the dopant atoms and the proton conductivity [10, 27]. Other studies suggest a more complex picture, where the fact that the use of one type of dopant or another one results in different proton conductivity has been associated with the disorder each kind of dopant introduces in the host lattice and its effect on the electronic structure [11]. Recent X-ray absorption spectroscopy investigations of the local structure of acceptor doped BaZrO₃ by Giannici *et al.* [11, 31, 46] have suggested that those dopants which give rise to the highest proton conductivity, *e.g.* Y³⁺, are the ones which introduce high local disorder and have low solubility in the host matrix. Accordingly, they proposed that the In³⁺ cation mimics the doped atom (Zr⁴⁺), while the Y³⁺ cation acts as a rigid inclusion in the host lattice. Contrarily to Y-doping, In-doping seems, even at high concentration, to not introduce pronounced distortions or structural rearrangement in the BaZrO₃ structure [25, 31]. This effect has been suggested as a possible reason for the lower conductivity of In:BZO with respect to the one of Y:BZO [31].

Considering the effect of acceptor doping on the elementary transport steps, some studies have proposed that the proton sites close to the dopant atoms act as trapping sites [27, 31, 34, 60]. However, it has been also suggested that the presence of the In atoms affect the proton transport in a more non-localized way [33]. Furthermore, it is important to notice that the formation and break-

ing of hydrogen bonds is highly important in the elementary transport steps. Therefore, it is of particular interest to study and understand the nature of the hydrogen bonds, which is strongly influenced by the local environment around the protons [11, 24, 32, 60]. The presence of dopant atoms is not the only factor that determines the local structure, as other defects may as well contribute. As an example, oxygen vacancies are well known structural defects which interact strongly with the protons in proton conducting oxides [Figure 1.4(c)] [50, 61]. The protons can be considered as charge defects, and the insertion of charged defects influences both the short- and long-range structure of the perovskite [56, 61], as it is shown, for example, by the expansion of the unit cell volume upon hydration [25, 26, 30, 55]. Proton-proton interaction may also be important in materials with a high concentration of protons [33]. To conclude, several aspects regarding the nature of the proton sites and their dynamics are still not fully understood. Their investigation lies at the heart of this thesis.

Chapter 2

Methods

2.1 Vibrational spectroscopy

Vibrational spectroscopy techniques are used to probe the local structure and vibrational dynamics in materials and have been used extensively in this thesis. Vibrational dynamics refer to oscillations of the atoms around their equilibrium positions, which are manifested as bands in a vibrational spectrum. The bands are characterized by their position (frequency), intensity and shape, which relate to the local structural arrangement of and around the vibrating species. The study of the vibrational spectrum can therefore provide useful information about the structure of a material, including, for example, the presence and nature of local structural distortions or structural defects. In a simplified, harmonic, description the frequency of a vibrational mode is given by $\omega \propto \sqrt{F/\mu}$, where F is the strength of the bonds between the atoms and μ is the reduced mass of the oscillating unit. The band-width relates to how well defined the vibration is, whereas the band-intensity relates to the number of vibrating species.

Vibrational spectroscopy techniques may be divided in those which rely on the absorption of a photon at the energy of the vibration, *e.g.* infrared (IR) spectroscopy, and those which rely on inelastic scattering, *e.g.* Raman and inelastic neutron scattering (INS). In this work, IR and INS spectroscopy were used. A brief description about these techniques is given in the following.

2.1.1 Infrared spectroscopy

¹IR spectroscopy is based on the interaction between IR radiation, $\lambda \in [700 \text{ nm} - 1 \text{ mm}]$, and matter. When the energy of the incident light matches the energy of a vibrational mode, the light can be absorbed, which is manifested as an absorbance band in a vibrational spectrum. Therefore, a measurement of the absorption (or the transmission) of the sample as a function of the frequency of the incident light gives information about the vibrational modes characteristic of the sample.

On a fundamental level, the interaction between matter and electromagnetic radiation can be described as a resonant interaction, where the electromagnetic radiation induces a change in the dipole moment, $\boldsymbol{\mu}$, which is a function of the atomic charges (e_i) and the relative atomic positions (\mathbf{r}_i) of the vibrating moiety

$$\boldsymbol{\mu} = \sum_i e_i \mathbf{r}_i. \quad (2.1)$$

The measured intensity of a vibrational band is proportional to the square of the change in the dipole moment ($d\boldsymbol{\mu}/dq$). Vibrational modes which are not causing any change in the dipole moment are therefore normally not observable with IR spectroscopy.

2.2 Inelastic neutron scattering

A neutron scattering experiment is characterized by the use of neutrons as probing particles, *i.e.* the properties of a sample are studied by investigating how the neutrons are scattered from the sample. Neutrons have no electric charge and their interaction with matter occurs *via* scattering on the atomic nuclei. Neutrons display a wave-particle duality and can exchange both energy and momentum upon the scattering on a sample. The interaction is generally weak, which makes neutrons a deeply penetrating probe and hence suitable for the investigation of bulk properties of materials. The strength of the neutron-nucleus interaction is described by the scattering cross section σ or the scattering length b , where $\sigma = 4\pi b^2$ is expressed in barns (1 barn = 10^{-24} cm^2). Since neutrons have a magnetic spin, they can also interact magnetically with matter, but this interaction can be neglected in the case of non-magnetic materials, as the ones studied here.

¹A more exhaustive introduction to IR spectroscopy can be found in several textbooks, *e.g.* Refs. [62–64].

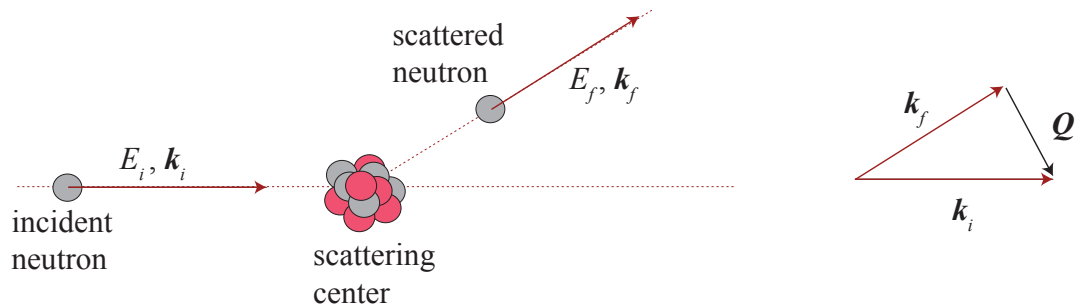


Figure 2.1: Schematic illustration of the scattering process for a neutron, as described in the text.

In a neutron-nucleus scattering event [Figure 2.1] the initial state (i) and final state (f) of the neutron are described by its momentum, \mathbf{k}_i and \mathbf{k}_f ,² and energy,

$$E_i = \frac{\hbar}{m_N} k_i^2, \quad E_f = \frac{\hbar}{m_N} k_f^2,$$

where m_N is the mass of a neutron. The measurable quantity in most of the neutron scattering experiments is the intensity of the scattering as a function of the exchanged energy, $\hbar\omega = E_i - E_f$, and the exchanged momentum, $\mathbf{Q} = \mathbf{k}_i - \mathbf{k}_f$. The intensity is usually expressed as a function of the double differential cross section $d^2\sigma/dE_f d\Omega_f$, *i.e.* the number of scattered neutrons in the solid angle $d\Omega$ in the energy interval dE_f , divided by the incident neutron flux.

The scattering can be divided into elastic and inelastic scattering, depending on if the neutrons exchange energy with the sample (inelastic) or not (elastic). When there is interference among the scattered neutron waves, the scattering is referred to as coherent. Coherent scattering contains information about the structure (elastic case), as in neutron diffraction, and/or about collective motions of atoms (inelastic case). Incoherent scattering arises when disorder reduces or destroys the interference between scattered neutron waves. In this case, the scattering does not contain information about correlations, *i.e.* how different atoms are distributed or move with respect to each other, but can probe the properties of individual atoms, such as proton self-dynamics in acceptor doped BaZrO₃.

Of specific concern in this thesis is the investigation of vibrational, incoherent, proton dynamics by means of INS measurements. The following description is thus developed in the framework of the incoherent approximation, were

²In this thesis tensorial quantities are indicated in bold, as for example \mathbf{k}_i , \mathbf{k}_f and \mathbf{Q} . The norm of a vector \mathbf{k} is simply indicated by $k = |\mathbf{k}|$.

the dynamic response is calculated treating all the scattering as incoherent but using the total scattering cross section [65]. The double differential scattering cross section may be then expressed as

$$\left. \frac{d^2\sigma}{dE_f d\Omega_f} \right| = \frac{1}{2\pi\hbar} \sum_l S(\mathbf{Q}, \omega)_l = \sum_l \frac{\sigma}{2\pi\hbar} \int dt \langle e^{-i\mathbf{Q}\cdot\mathbf{r}_l(0)} e^{i\mathbf{Q}\cdot\mathbf{r}_l(t)} \rangle e^{-i\omega t}, \quad (2.2)$$

where l labels the different atomic species and \mathbf{r}_l is the time dependent atomic position. S is known as the scattering law, or dynamical structure factor. In the specific case of vibrational modes of hydrogenous systems, S can be rewritten as³

$$S(Q, \omega_\nu)_l^{(n)} \propto \frac{\sigma_l}{n!} \int [(\mathbf{Q}\mathbf{Q}^T) : \mathbf{B}_{l,\nu}]^n e^{-[(\mathbf{Q}\mathbf{Q}^T) : \mathbf{A}_l]^2} d\mathbf{Q}, \quad (2.3)$$

where $\mathbf{u}_{l,\nu}$ is the displacement vector of the atom l along the direction of the vibrational mode ν , $\mathbf{B}_{l,\nu} = \mathbf{u}_{l,\nu}^T \mathbf{u}_{l,\nu}$ is the mean square displacement tensor, $\mathbf{A}_l = \sum_\nu \mathbf{B}_{l,\nu}$ is the total mean square displacement, and the operator $:$ implies the calculation of the trace of the matrix obtained as the tensorial product between the left and the right side terms. Here $n = 1$ indicates fundamental modes, $n = 2$ their first overtones, $n = 3$ their second overtones, and so forth.

Despite the analytical complexity of Eq.(2.3), information about the behaviour of $S(Q, \omega)$ can be derived by observing the results in Figure 2.2, which shows, as an example, the theoretical Q -profiles and the INS spectrum of hydrated 50In:BZO [see Paper II]. The theoretical Q -profiles were calculated in agreement with Eq.(2.3) for typical O–H frequencies in this material.⁴ If $Q^{(max)}$ is the value of Q which maximizes $S(Q, \omega)$, then it can be inferred that $Q^{(max)}$ increases as (i) the energy of a mode, $\hbar\omega_\nu$, increases and (ii) as the order of the transition, n , increases.

The analytical expressions of $S(Q, \omega_\nu)_l^{(n)}$ can be sometimes simplified [65, 68]. For instance, when $|\mathbf{u}_{l,\nu}| = \bar{u}_l \forall \nu$ (isotropic oscillator) the expression in Eq.(2.3) becomes analytically less complex and it can be shown that

$$Q^{(max)} = \sqrt{n} (\bar{u}_l)^{-1} \forall \nu.$$

³The complete derivation of the following results can be found in Ref. [65] and is based on the assumptions that (i) all modes are dynamically decoupled, (ii) the scattering can be described as completely incoherent and (iii) $2k_B T / \hbar\omega \ll 1$. For a more general derivation the reader may consult Refs. [66, 67].

⁴The mean square displacements were calculated for O–H vibrations with energies 67, 106 and 444 meV [24] under the assumption of harmonic behaviour, *i.e.* $u_\nu^2 = \hbar / (2\mu_\nu\omega_\nu)$, where μ_ν is the reduced mass of the O–H vibrating unit.

The study of the Q dependence of S provides therefore a useful analytical method to distinguish between fundamental modes ($n = 1$) and higher-order transitions ($n \geq 2$) [65], and it has been used successfully for the assignment of the vibrational spectra of Rb_2PtH_2 and Rb_2PtD_6 [69] and KH_2AsO_4 [70].

At this point, it is important to remark some differences between INS and optical spectroscopy. First, unlike optical spectroscopy, in INS all vibrations are active, and, in principle, measurable. Moreover, neutron techniques are not limited to the observation of vibrational modes at the Brillouin zone centre, and the intensity of the measured INS spectrum is proportional to the population of the vibrational species present in the sample. However, one should notice that the existence of selection rules in the optical techniques can be used as an advantage, as for example in the identification of intrinsic defects or symmetry breaking in crystalline materials [29, 34, 46, 71].

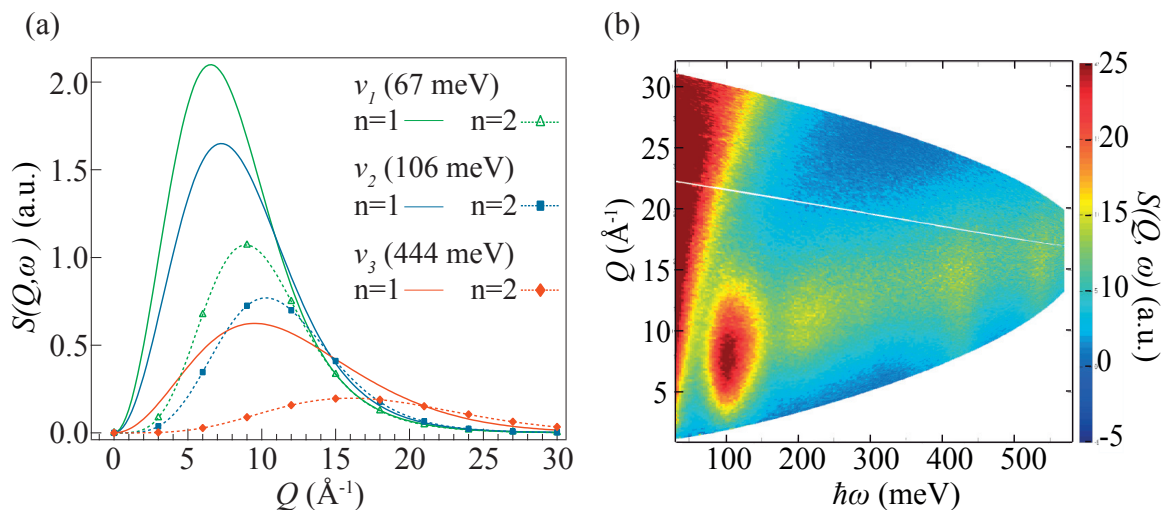


Figure 2.2: (a) Theoretical Q -profiles for fundamental harmonic O–H vibrations ($n = 1$) and their overtones ($n = 2$) [24]. (b) INS spectrum of hydrated $\text{In}_{50}\text{:BZO}$ powder [Paper II]. Notice how the maximum in intensity occurs at higher Q when the energy of the mode or the order of the transition increases.

2.3 X-ray and neutron reflectivity

⁵Reflectivity experiments are based on the study of the interference between reflections of the probing beam coming from different interfaces in a material. When a beam (neutron or X-ray) hits the interface between the vacuum and a medium at an incident angle θ [Figure 2.3(a)] one part of the beam is refracted at an angle θ_R according to Snell's law

$$n_0 \cos(\theta) = n_1 \cos(\theta_R), \quad (2.4)$$

where n_1 is the refractive index of the medium and $n_0 = 1$ is the one of the vacuum. The refractive index contains information about the interaction between the medium and the radiation (neutrons or X-rays), and it can be expressed as $n = 1 - \delta - i\beta$, where δ and β take into account the refraction and the absorption phenomena, respectively. Here the absorption term will be ignored, and the following description concerns only the term δ_{XR} , for X-ray diffraction, and δ_N , for neutron diffraction, which can be expressed as

$$\delta_{XR} = \frac{r_e \rho_e \lambda^2}{2\pi} = \frac{\lambda^2}{2\pi} \cdot eSLD \quad (2.5)$$

and

$$\delta_N = \frac{b\rho\lambda^2}{2\pi} = \frac{\lambda^2}{2\pi} \cdot nSLD, \quad (2.6)$$

respectively. ρ_e is the number of electrons per unit volume, r_e is the classical radius of the electron, ρ is the atomic density and b is the coherent neutron scattering length. $eSLD$ and $nSLD$ are the electronic and neutron scattering length densities, respectively.

Specular reflectivity measurements probe the depth profile of the SLD by measuring the absolute reflectivity $R(\theta)$, *i.e.* the ratio between the reflected and incident intensities as a function of the incident angle. Sometimes it is suitable to express the reflectivity as a function of the modulus of the transferred wave vector, $Q_z = 2k_z = 4\pi \sin(\theta)/\lambda$, where λ is the wavelength of the incident radiation. The absolute reflectivity $R(Q_z)$ can be calculated by solving the equations describing the propagation of radiation and using proper boundary conditions at the interfaces. In the following the case of the reflectivity process from two interfaces, illustrated in Figure 2.3(b), will be considered, under the assumptions $n_0 = 1$, $n_1 < 1$, and $n_2 < 1$. A characteristic feature of

⁵The following introduction to the basic principle on reflectivity is mainly after Ref. [72].

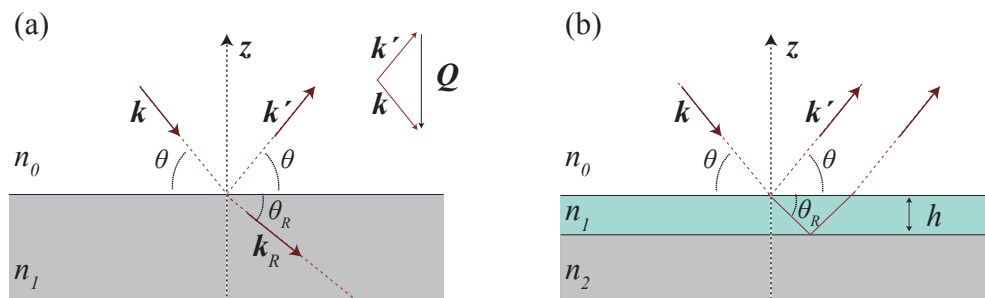


Figure 2.3: Schematic depiction of the reflectivity process from a single interface (a) and two interfaces (b). \mathbf{k} , \mathbf{k}' and \mathbf{k}_R are the wavevectors of the incident, reflected and refracted waves, θ and θ_R are the angles of incidence and refraction, and $\mathbf{Q} = \mathbf{k} - \mathbf{k}'$ is the transferred wavevector.

any reflectivity curve is the existence of a critical angle θ_c such that $R(\theta) = 1$ for $\theta < \theta_c$. The critical angle can be calculated from $\cos(\theta_c) = n$, where n is the smallest between n_1 and n_2 . At small angle, and if absorption is ignored, the absolute reflectivity can be then written as

$$R(Q_{z,1}) = \frac{r_{0,1}^2 + r_{1,2}^2 + 2r_{0,1}r_{1,2} \cos(Q_{z,1}h)}{1 + r_{0,1}^2 r_{1,2}^2 + 2r_{0,1}r_{1,2} \cos(Q_{z,1}h)}, \quad (2.7)$$

where

$$r_{0,1} = \left| \frac{Q_{z,1} - \sqrt{Q_{z,1}^2 - Q_{c,2}^2}}{Q_{z,1} + \sqrt{Q_{z,1}^2 - Q_{c,1}^2}} \right|, \quad r_{1,2} = \left| \frac{Q_{z,2} - \sqrt{Q_{z,2}^2 - Q_{c,2}^2}}{Q_{z,2} + \sqrt{Q_{z,2}^2 - Q_{c,2}^2}} \right|, \quad (2.8)$$

and

$$Q_{z,1} = 4\pi \sin(\theta)/\lambda, \quad Q_{z,2} = 4\pi \sin(\theta_R)/\lambda. \quad (2.9)$$

$r_{0,1}$ and $r_{1,2}$ are the reflection coefficients at the interfaces 0–1 and 1–2, Q_c is the critical Q -value ($\approx 4\pi\theta_c/\lambda$), and h is the thickness of the layer. $R(Q_{z,1})$ decays as the fourth power of Q_z and the oscillating term of periodicity $\Delta Q_{z,1} = 2\pi/h$ is due to multiple reflections at the interfaces and induces oscillations in the reflectivity curves referred to as Kiessig fringes.

Increasing the complexity of the structure, *e.g.* by introducing more than two layers, an uneven depth profile, roughness at the interfaces, and absorption in the film, the expression of specular reflectivity becomes analytically more challenging and the interpretation less straightforward. In 1954, Parrat proposed a recursive method that yields the *SLD* as a function of depth in layered

structures [73]. In Figure 2.4 are shown theoretical X-ray reflectivity (XRR) curves for a 50 nm layer of 50In:BZO on top of an infinite MgO substrate. The corresponding Kiessig fringes have a period of $\approx 0.012 \text{ \AA}^{-1}$, and the critical Q_z value is $Q_c \approx 0.05 \text{ \AA}^{-1}$. The effects of increasing surface roughnesses are a steeper decay of the reflectivity curve and a damping of the Kiessig fringes. A real example of a XRR curve is shown in Figure 2.5 for a 50 nm thin film of 50In:BZO on a MgO substrate. In this case a beating in the curve arises due to the presence of an inhomogeneity in the $eSLD$, which is shown in the insert of Figure 2.5.

In a typical reflectivity experiment one would generally like to obtain information about the thickness and composition depth profile in the studied sample. The depth profile of the scattering length density, $SLD(z)$, can be interpreted as a composition depth profile when the scattering lengths of the constituent atoms are known. The $eSLD(z)$ and $nSLD(z)$ may be expressed as

$$eSLD(z) = \sum_{i=1}^m f_i \rho_i(z) \quad (2.10)$$

and

$$nSLD(z) = \sum_{i=1}^m b_i \rho_i(z), \quad (2.11)$$

where $\rho_i(z)$, f_i and b_i are the number density, the electronic scattering factor and coherent neutron scattering length of the atomic species i .

In this thesis, XRR has been used to determine the composition depth profile of hydrated, deuterated and dehydrated films of In:BZO, whereas NR has been used on a complementary basis to obtain details on the composition depth profile of the hydrogen and deuterium atoms. A key property of NR exploited in this thesis is the large neutron cross section of hydrogen and deuterium, and the large contrast between the coherent scattering length densities of these two elements,⁶ meaning that NR is highly sensible to the hydrogen/deuterium insertion and desorption.

⁶The coherent scattering lengths and cross sections for hydrogen are $b_H = -3.7390 \text{ fm}$ and $\sigma_H = 1.7568 \text{ barns}$, respectively, and for deuterium $b_D = 6.71 \text{ fm}$ and $\sigma_D = 5.592 \text{ barns}$, respectively.

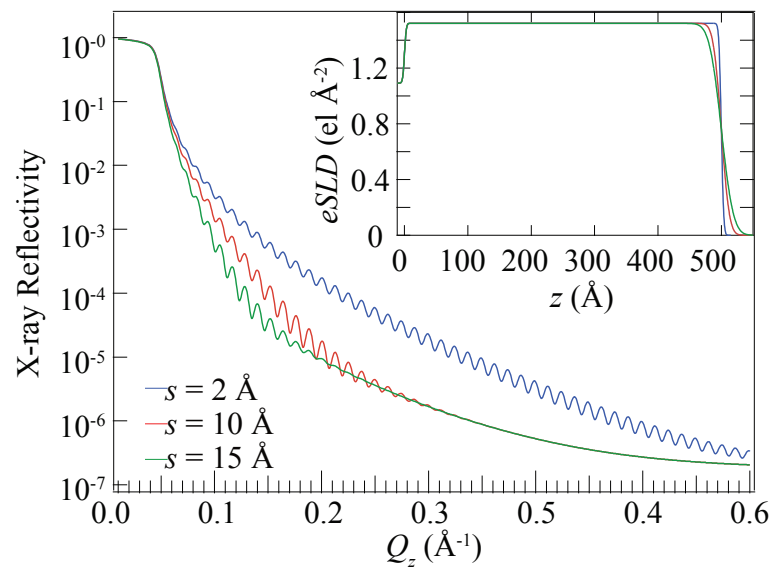


Figure 2.4: XRR curves for three different surface roughnesses, s , generated for a uniform layer of 50In:BZO on top on an infinite MgO substrate using the GenX software [74]. The corresponding $eSLD$ profiles are shown in the insert.

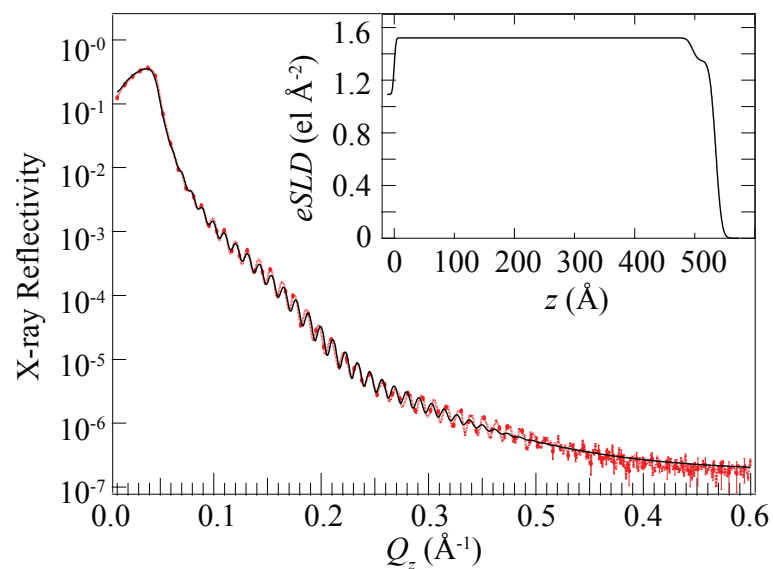


Figure 2.5: XRR curve as measured on a thin film ($\approx 50 \text{ nm}$) of 50In:BZO on MgO substrate, together with the best fit and the calculated $eSLD$ profile [Paper III].

2.4 Nuclear reaction analysis

⁷Nuclear reaction analysis (NRA) *via* the ${}^1\text{H}({}^{15}\text{N},\alpha\gamma){}^{14}\text{C}$ reaction is a technique that can be used to determine the hydrogen content and depth profile inside a material. The nuclear resonant reaction between nitrogen nuclei, ${}^{15}\text{N}$, and (target) hydrogen nuclei, ${}^1\text{H}$, occurs when the ${}^{15}\text{N}$ atoms are accelerated to the resonance energy $E_R = 6.385$ MeV. The product of the reaction are β and γ -rays, which are ejected from the target.⁸ The produced γ -rays are characterized by an energy of ≈ 4.4389 MeV, and their amount is directly proportional to the concentration of hydrogen atoms in the sample. Depth profiling can be achieved by accelerating N nuclei to energies $E_N > E_R$. ${}^{15}\text{N}$ atoms with energy $E_N = E_R$ will undergo the nuclear reaction with ${}^1\text{H}$ close to the surface of the target. Those with $E_N > E_R$ will instead penetrate into the sample and experience energy loss because of their interaction with electrons, which is described by the electronic stopping power s . The energy loss (ΔE) is proportional to the trajectory length in the sample, z , and the stopping power. In a simplistic description, when the ${}^{15}\text{N}$ atoms reach the resonance energy, *i.e.* $\Delta E(z) = E_N - E_R$, the reaction can occur. The γ count rate, $I_\gamma(E_N)$, as a function of the energy of the nitrogen beam can be expressed as

$$I_\gamma(E_N) \propto \int \delta(E_N - E_R - z \cdot s) n_H(z) dz, \quad (2.12)$$

where $n_H(z)$ is the concentration profile of the hydrogen in the target. In a more realistic description, the δ function in the expression above has to be replaced by the Lorentzian-shaped cross section of the reaction. One should also consider the ion beam energy distribution around the nominal energy E_N . Furthermore, the energy distribution increases while the ${}^{15}\text{N}$ nuclei travel inside the material, due to the stochastic nature of the interaction with the electrons. Thus, the γ count rate can be expressed as

$$I_\gamma(E_N) \propto \int F(E_N, z) n_H(z), \quad (2.13)$$

where F is an effective instrumental function. As an example, the NRA spectrum of hydrated 50In:BZO is shown in Figure 2.6. $I_\gamma(E_N)$ was converted into relative hydrogen content, n'_H , as a function of z . The absolute concentration

⁷Here it follows a description of the basic principles of nuclear reaction analysis, mainly after the approach of Ref. [75].

⁸The complete nuclear reaction is ${}^1\text{H} + {}^{15}\text{N} \rightarrow {}^{16}\text{O} \rightarrow {}^{12}\text{C} + \alpha + \gamma$, which involves the creation, in the intermediate step, of an unstable ${}^{16}\text{O}$ nucleus.

of ^1H can be obtained by using the measurements of a reference sample with known composition and H content. In this respect, it should be noted that the precision of NRA measurements is influenced by the quality and the uncertainty about the calibration sample serving as a reference, which often leads to an uncertainty of as much as 10%. However, the accuracy of the method is extremely high and only limited by the statistical uncertainty related to the γ count rate.

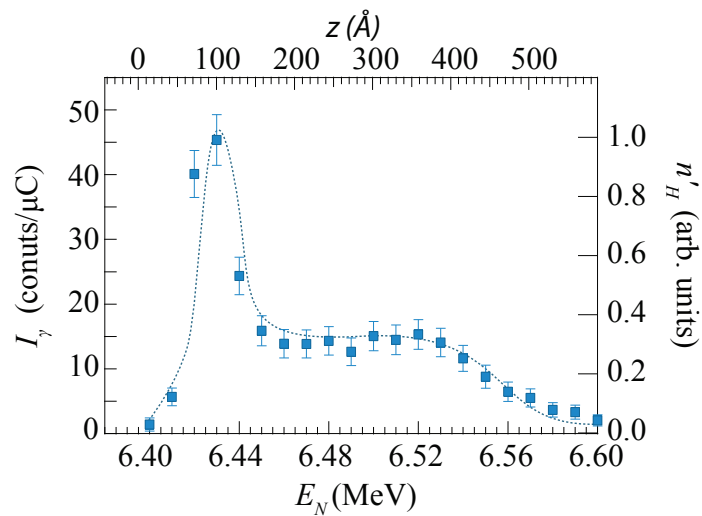


Figure 2.6: γ -ray count rate, $I_\gamma(E_N)$, and relative hydrogen content depth profile, $n'_H(z)$, as measured on a hydrated 50In:BZO film [Paper III].

Chapter 3

Instrumentation

3.1 The MERLIN and TOSCA spectrometers

In this thesis two different time-of-flight (TOF) INS spectrometers were used, MERLIN [Figure 3.1] and TOSCA [Figure 3.2], both available at the ISIS Pulsed Neutron and Muon Source (STFC Rutherford Appleton Laboratory, U.K.).¹ MERLIN is a direct geometry spectrometer, meaning that the energy of the incoming neutrons is fixed, and the INS intensity is measured for different final energies. MERLIN is suitable for simultaneous measurements of transferred momentum (Q) and transferred energy ($\hbar\omega$) and, compared to other INS spectrometers, is characterized by a large incident flux and a large detector area which offers the possibility to explore a large Q -range [77]. The energy of the incident neutrons can be chosen in a large range, from 7 to 2000 meV [77]. TOSCA is an indirect geometry spectrometer, *i.e.* working with fixed final energy, suitable for INS measurements with transferred energy between 0 and 1000 meV [78]. The scattered neutrons are detected on five forward detector banks, at 47.5° , and five backward detector banks, at 132.3° [78]. While MERLIN has a resolution of the order of 3-5% of the incident energy [77] and therefore it is not suitable for high-resolution experiments, TOSCA has a resolution of the order of 1% of the transferred energy [78] and therefore is suitable for high-resolution measurements at low energy. In relation to the work summarized in this thesis [Paper I and II], MERLIN allowed the investigation of the entire range of the O–H vibrational dynamics [50-800 meV], including both fundamental vibrational modes and their overtones, with medium resolution, whereas the better resolution of TOSCA at low energies was employed

¹Exhaustive descriptions of the different types of INS spectrometers and their characteristics can be found in literature, *e.g.* [65, 76].

for a more detailed investigation of the O–H wag region [50–200meV].

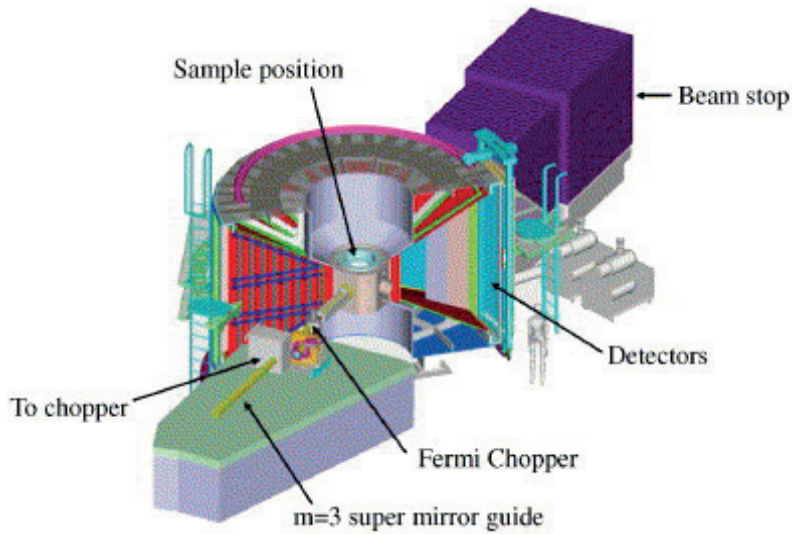


Figure 3.1: Schematic view of the MERLIN spectrometer at ISIS, taken from Ref. [79].

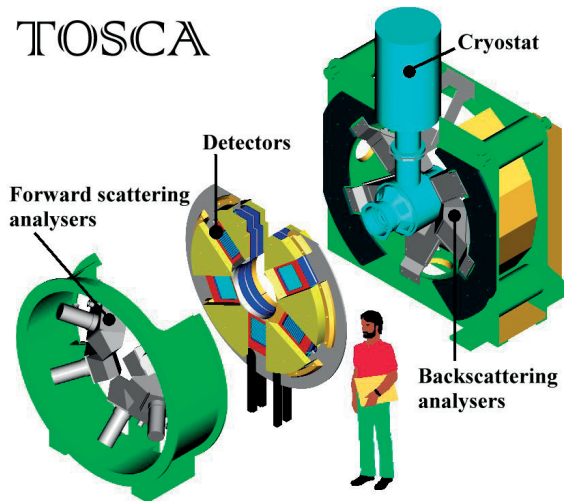


Figure 3.2: Schematic view of the TOSCA spectrometer at ISIS, taken from Ref. [79].

3.2 IR spectrometers

The IR spectra reported in this thesis [Paper I] were measured on a Bruker Alpha Fourier Transform IR (FTIR) spectrometer in diffuse reflectance configuration.² An FTIR spectrometer consists of three main components: a source of polychromatic IR radiation, an interferometer and a detector (see Figure 3.3). The polychromatic light is divided into two beams where one is transmitted to the moving mirror and the other one is reflected to the fixed mirror. The light is then reflected off both mirrors and both beams arrive on the sample and, subsequently, on the detector. The path difference between the two beams is varied by changing the position of the moving mirror and an interference pattern is recorded as a function of this path difference. Fourier transformation of the interference pattern yields a vibrational spectrum, *i.e.* intensity *vs* frequency [63, 64, 80]. Measurements can be performed in two modes of operation: reflectance (specular or diffuse) and transmittance (see Figure 3.3). Measurements in diffuse reflectance mode, as the ones performed in this thesis, are most suitable for measurements on powders and are realized by blocking the specularly reflected light.

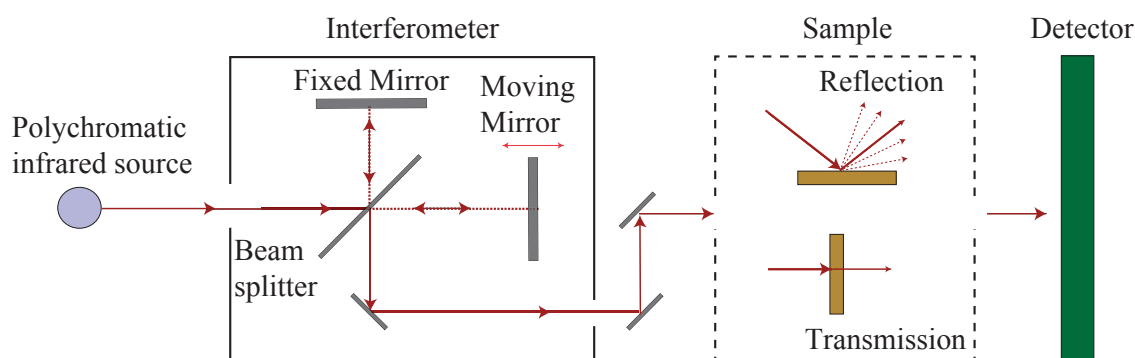


Figure 3.3: Simplified scheme of a FTIR spectrometer. The sample is located between the interferometer and the detector. Depending on the modes of operation, the radiation can be either reflected or transmitted by the sample.

²It is beyond the aim of this work to give an exhaustive description of these instruments. More information and details can be found elsewhere [63, 64].

3.3 Neutron reflectometers

Neutron reflectometers can be divided into two main groups of instruments: monochromatic instruments and TOF instruments. In the first case, neutrons with a specific wavelength (λ) are used and the reflectivity is measured at the specular condition as a function of the incident angle θ by rotating both the sample and the detector (see Figure 3.4). In TOF measurements the incident angle θ is fixed and a polychromatic pulsed beam is used. The traveling time Δt over a distance ΔL is inversely proportional to the transferred momentum Q_z through the relationship

$$\Delta t = \frac{\Delta L}{v} = \Delta L \cdot \frac{m_N}{h} \cdot \frac{4\pi \sin(\theta)}{Q_z},$$

where m_N is the mass of the neutron. The reflectivity data is collected as a function of the TOF of the neutrons and converted to $R(Q_z)$.

For the NR experiments in this thesis [Paper III], two different instruments were used: the polarized beam reflectometer (PBR) at the NIST Center for Neutron Research (NCNR) and the D17 reflectometer at the Institut Laue-Langevin (ILL). PBR is a horizontal-geometry polarized beam reflectometer equipped with a monochromatic beam of a wavelength of $\lambda = 4.786 \text{ \AA}$ [81, 82]. D17 is a horizontal-geometry reflectometer that allows measurements in both monochromatic and TOF mode [83, 84]. Using a TOF instrument it is possible to collect data over a fairly large Q -range in a short time. In this thesis, NR experiments were performed during and after heating and cooling cycles and the use of D17 in the TOF operation mode allows the monitoring of fast changes in the reflectivity curves, although with low statistics. This is important, for instance, to catch sight of fast changes in the chemical composition of the sample upon dehydration. However, in our work, measurements at high Q_z values ($Q_z > 0.1 \text{ \AA}^{-1}$) were needed, and, in this respect, the main drawback of the TOF instruments is that the simultaneous measurements over a large Q -range usually result in reflectivity data having different statistics at low and high Q_z values. Using monochromatic instruments, such as the PBR reflectometer, it is possible to set different measuring times for different Q_z values, thus obtaining similar statistics in the majority of the Q -range.

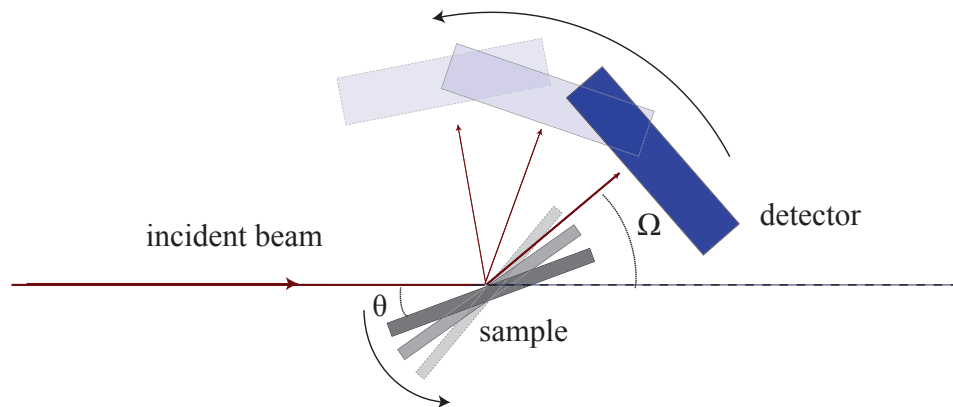


Figure 3.4: Schematic top view of a vertical-sample geometry reflectivity set-up, where the two independent rotational movements of the sample (θ) and of the detector (Ω) are indicated. The specular condition is obtained for $\Omega = 2\theta$.

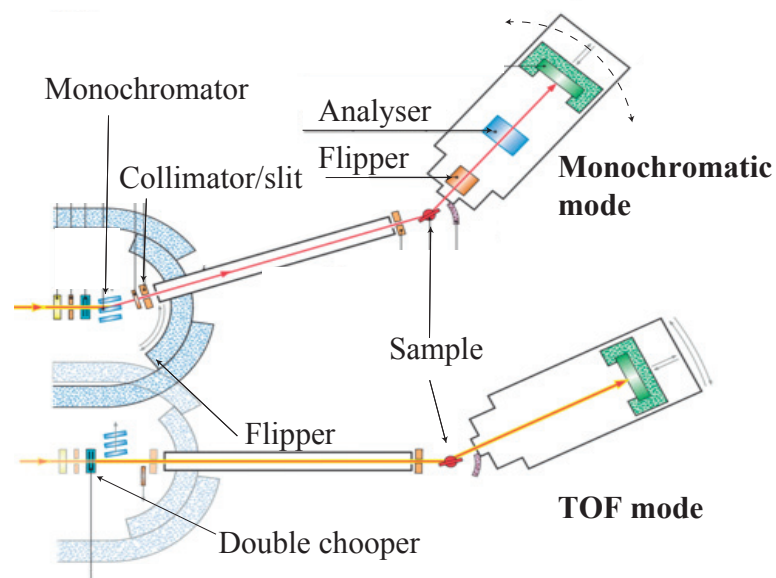


Figure 3.5: Schematic top view of the D17 reflectometer, adapted from Ref. [83].

Chapter 4

Summary of results

4.1 Paper I

This paper concerns the investigation of structure, vibrational dynamics and nature of the proton sites in 10In:BZO. Our results show that the vibrational dynamics and the strength of the hydrogen bonding associated with a specific proton site can be related to the local arrangement of the In/Zr atoms. In particular, we found that the hydrogen bond is weaker for proton sites located close to the In atoms. We also found that the strength of the hydrogen bonds relates to the tilting of the InO_6 / ZrO_6 octahedra, and not, as often suggested in literature, to the tilting of the O-H covalent bond. Our findings suggest that the proton vibrational spectrum is dominated by the vibrational dynamics associated to configurations where the protons are “trapped” close to the In atoms.

The investigations were performed using *ab initio* MD simulations and INS spectroscopy. MD simulations were performed at $T = 100$ K, thus hindering proton diffusion events and ensuring the probing of unique proton sites and their vibrational dynamics. More specifically, three representative different proton configurations were selected for the simulations, in order to probe the effect of the In-H distance on the O-H vibrational dynamics. Complementary INS measurements on a polycrystalline sample of 10In:BZO were performed in a very broad range of transferred energy (0–1000 meV) using the MERLIN spectrometer at the ISIS Pulsed Neutron and Muon Source.

4.2 Paper II

In this paper we have investigated the vibrational dynamics and the nature of the proton sites in 50In:BZO. The results show the presence of several different types of proton sites in the material, each one characterized by a different strength of hydrogen bonding and vibrational dynamics. In particular, the results point towards the presence of a growing population of proton sites characterized by stronger hydrogen bonding with respect to those present at lower doping level. The strength of the hydrogen bonding and the vibrational dynamics associated to each proton site appear to be independent on both the Zr/In local arrangement and the H-H distance. The proton trapping effect around the In atoms appears to be “removed” or hindered due to the high concentration of dopant atoms.

The paper is based on experimental and computational results. INS and IR spectroscopy were used to investigate the vibrational spectra of a polycrystalline sample of 50In:BZO. INS measurements were performed in a very broad range of transferred energy (0–1000 meV) using the MERLIN and TOSCA spectrometers. MERLIN was employed for the analysis of the Q -dependence, whereas TOSCA was employed for higher resolution measurements. MD simulations were performed at $T = 100$ K on several different proton configurations, in order to probe the effects of the In-H/H-H distance on the O-H vibrational dynamics.

4.3 Paper III

In this paper we reported the results of our study on epitaxial thin films (≈ 50 nm) of 50In:BZO, which reveal the presence of a thin, 3-4 nm thick, near-surface region in the samples, characterized by an excess of protons and an altered cationic composition. Whereas the bulk of the sample showed none or negligible grain-boundary contribution to the proton conductivity, due to the high crystallinity of the film, and was found to absorb and desorb protons in the expected manner, the near-surface region either retains protons upon desorption or re-obtains them after it. A comparison between our findings, published IR spectra and quasielastic neutron scattering data suggests that the near-surface region is characterized by a reduced proton mobility and proton sites associated with relatively weak hydrogen bonds. In effect, this indicates that strong hydrogen bonding is favorable for high proton mobility.

The investigations were performed using a combination of XRR, NR, NRA, RBS and IS. XRR, NR and NRA measurements were performed on both nomi-

nally fully hydrated and dehydrated samples, in order to investigate any effects upon dehydration. XRR was used to determine the composition depth profile of the perovskite matrix, whereas NR and NRA were used to obtain details on the concentration depth profile of the hydrogen atoms. RBS and IS measurements were performed in order to obtain information about the sample composition and proton mobility.

Chapter 5

Conclusions and Outlook

The behavior of protons in acceptor doped proton conducting oxides is an important and interesting research topic in the field of materials for energy applications and of relevance for the development of IT-SOFC technology. As it has been discussed in the previous chapters, there are still several open questions regarding the mechanistic aspects of the proton local dynamics. In this context, this thesis has provided important new insights about the coupling between structure, local environment and conductivity in proton conducting oxides. In particular, it has been shown how the increase of the doping level has important effects on the vibrational dynamics, hydrogen bonding and population of the different types of proton sites in In-doped BaZrO₃. While for low doping levels the proton sites can be fully characterized by the local arrangements of the In/Zr atoms, some of which lead to the formation of proton trapping sites where the protons are energetically more stable, this is not the case at higher doping levels. Our work has shown that trapping sites appear to be characterized by the weakest hydrogen bonding. Furthermore, our study of thin film samples has revealed the presence of a proton-enriched surface region, characterized by an anomalous hydration/dehydration behavior. It has been suggested that the proton sites in the surface region are characterized by reduced mobility.

Besides being both of fundamental interest and of relevance for future IT-SOFCs in actual operations, the results in this thesis demonstrate the applicability and potential of (i) INS, IR and MD simulations in providing important details about the nature of the proton sites in oxides and (ii) NR, XRR and NRA for gaining unique insight into the structural properties of proton conducting oxide materials. Furthermore, the studies presented here highlight the unique advantage of using neutron scattering techniques when investigating

materials containing hydrogen atoms.

With a view into the future, I see a lot of possibilities to build further on the studies presented in this thesis. Concerning the investigations presented in Paper I and II, it still remains to be clarified the importance of the trapping effect in the proton conduction process in In-doped BaZrO₃, as well as the role of the doping level. Future works may include a wider range of doping levels, which would allow a better understanding of the role of the In-doping. Conductivity and nuclear magnetic resonance experiments should also be performed in the future. The first may provide a direct comparison between the short-range properties, such as the vibrational dynamics, and the long-range proton mobility, whereas the second will provide complementary information about the nature of proton sites. Since the choice of the type of dopant atom strongly influences the conductivity of BaZrO₃ based proton conducting oxides, future studies will be extended to different dopant atoms. The primary aim of such studies is to investigate the correlation between the macroscopic changes in the proton conductivity and the vibrational dynamics and local structure in the materials.

Regarding the study of thin films, the investigations presented here could not achieve an exhaustive characterization of the proton sites in the near-surface region and their coupling with structural inhomogeneities. In this respect, more detailed structural characterizations of the films may be performed in future works. The absorption/desorption mechanism of the protons in the surface region remains also to be investigated in more detail, in particular in order to discriminate whether the protons, or a fraction of the protons, are retained during dehydration or re-absorbed after dehydration and cooling to room temperature. NR and NRA measurements during *in situ* hydration and dehydration, as well as on partially hydrated/dehydrated samples may be used to achieve this goal. Generally, these investigations could provide new insights not only on the nature of the proton sites, but also on other aspects, such as the conductivity at the grain boundary, which are of importance for practical applications.

Finally, we are considering the possibility to further investigate the role of the O-H vibrational dynamics on the transport process by using a similar approach to the one proposed by Sphar *et al.* [57,58] and discussed in Chapter 1, *i.e.* investigating thin film samples by means of the transient bleaching technique measurements combined with IR spectroscopy measurements. Overall, these studies may lead to important repercussion in the understanding of the mechanistic details of structure and dynamics in these technologically important materials.

Acknowledgments

I would like to start by thanking my supervisor, Maths Karlsson, for giving me the possibility to do my PhD at Chalmers and for the support and the resources I had during these years. I want also to thank the entire KMF group, for the support, the interesting discussions and the friendly atmosphere. I would like to express separately my gratitude to Ezio, for his help and kindness and all the useful advices. I would like to thank all the people that I have worked with and that have helped me during the last three years. Finally, I would like to thank my family and friends, for they unconditional support and affection.

Bibliography

- [1] S. Dunn, “Hydrogen futures: toward a sustainable energy system,” *Int. J. Hydrogen Energy*, vol. 27, pp. 235–264, mar 2002.
- [2] B. C. Steele and A. Heinzl, “Materials for fuel-cell technologies.,” *Nature*, vol. 414, pp. 345–52, nov 2001.
- [3] J. L. Liu, S. Bashir, and J. Liu, *Advanced Nanomaterials and their Applications in Renewable Energy*. Elsevier, 2015.
- [4] K. Kreuer, “PROTON-CONDUCTING OXIDES,” *Annu. Rev. Mater. Res.*, vol. 33, pp. 333–359, aug 2003.
- [5] L. Malavasi, C. A. J. Fisher, and M. S. Islam, “Oxide-ion and proton conducting electrolyte materials for clean energy applications: structural and mechanistic features.,” *Chem. Soc. Rev.*, vol. 39, pp. 4370–87, nov 2010.
- [6] E. Fabbri, D. Pergolesi, and E. Traversa, “Materials challenges toward proton-conducting oxide fuel cells: a critical review.,” *Chem. Soc. Rev.*, vol. 39, pp. 4355–69, nov 2010.
- [7] J. A. Kilner and M. Burriel, “Materials for Intermediate-Temperature Solid-Oxide Fuel Cells,” *Annu. Rev. Mater. Res.*, vol. 44, pp. 365–393, jul 2014.
- [8] M. Karlsson, “Proton dynamics in oxides: insight into the mechanics of proton conduction from quasielastic neutron scattering.,” *Phys. Chem. Chem. Phys.*, vol. 17, pp. 26–38, jan 2015.
- [9] H. Iwahara, T. Yajima, T. Hibino, K. Ozaki, and H. Suzuki, “Protonic conduction in calcium, strontium and barium zirconates,” *Solid State Ionics*, vol. 61, pp. 65–69, may 1993.

- [10] K. Kreuer, S. Adams, W. Münch, A. Fuchs, U. Klock, and J. Maier, "Proton conducting alkaline earth zirconates and titanates for high drain electrochemical applications," *Solid State Ionics*, vol. 145, pp. 295–306, dec 2001.
- [11] F. Giannici, A. Longo, K. Kreuer, A. Balerna, and A. Martorana, "Dopants and defects: Local structure and dynamics in barium cerates and zirconates," *Solid State Ionics*, vol. 181, pp. 122–125, feb 2010.
- [12] M. Karlsson, I. Ahmed, A. Matic, and S. Eriksson, "Short-range structure of proton-conducting $\text{Ba}M_{0.10}\text{Zr}_{0.90}\text{O}_{2.95}$ ($M=\text{Y}$, In, Sc and Ga) investigated with vibrational spectroscopy," *Solid State Ionics*, vol. 181, pp. 126–129, feb 2010.
- [13] M. Karlsson, A. Matic, D. Engberg, M. E. Björketun, M. M. Koza, I. Ahmed, G. Wahnström, L. Börjesson, and S.-G. Eriksson, "Quasielastic neutron scattering of hydrated $\text{BaZr}_{0.90}\text{A}_{0.10}\text{O}_{2.95}$ ($A = \text{Y}$ and Sc)," *Solid State Ionics*, vol. 180, pp. 22–28, feb 2009.
- [14] D. Han, Y. Nose, K. Shinoda, and T. Uda, "Site selectivity of dopants in $\text{BaZr}_{1-y}\text{M}_y\text{O}_{3-\delta}$ ($M = \text{Sc}$, Y, Sm, Eu, Dy) and measurement of their water contents and conductivities," *Solid State Ionics*, vol. 213, pp. 2–7, apr 2012.
- [15] D. Han, K. Shinoda, S. Sato, M. Majima, and T. Uda, "Correlation between electroconductive and structural properties of proton conductive acceptor-doped barium zirconate," *J. Mater. Chem. A*, vol. 3, pp. 1243–1250, dec 2015.
- [16] D. Noferini, M. M. Koza, P. Fouquet, G. J. Nilsen, M. C. Kemei, S. M. H. Rahman, M. Maccarini, S. G. Eriksson, and M. Karlsson, "Proton Dynamics in Hydrated $\text{BaZr}_{0.9}\text{M}_{0.1}\text{O}_{2.95}$ ($M = \text{Y}$ and Sc) Investigated with Neutron Spin?Echo," *J. Phys. Chem. C*, 2016.
- [17] D. Beckel, A. Bieberle-Hütter, A. Harvey, A. Infortuna, U. Muecke, M. Prestat, J. L. M. Rupp, and L. Gauckler, "Thin films for micro solid oxide fuel cells," *J. Power Sources*, vol. 173, pp. 325–345, nov 2007.
- [18] E. Traversa, "Toward the miniaturization of solid oxide fuel cells," *Electrochem. Soc. Interface*, vol. 18, no. 3, p. 49, 2009.
- [19] E. D. Wachsman and K. T. Lee, "Lowering the temperature of solid oxide fuel cells.," *Science*, vol. 334, pp. 935–9, nov 2011.

- [20] J. H. Shim, T. M. Gür, and F. B. Prinz, “Proton conduction in thin film yttrium-doped barium zirconate,” *Appl. Phys. Lett.*, vol. 92, p. 253115, jun 2008.
- [21] D. Pergolesi, E. Fabbri, A. D’Epifanio, E. Di Bartolomeo, A. Tebano, S. Sanna, S. Licocchia, G. Balestrino, and E. Traversa, “High proton conduction in grain-boundary-free yttrium-doped barium zirconate films grown by pulsed laser deposition,” *Nat. Mater.*, vol. 9, pp. 846–52, oct 2010.
- [22] Y. B. Kim, T. M. Gür, H.-J. Jung, S. Kang, R. Sinclair, and F. B. Prinz, “Effect of crystallinity on proton conductivity in yttrium-doped barium zirconate thin films,” *Solid State Ionics*, vol. 198, pp. 39–46, sep 2011.
- [23] T. Higuchi, T. Owaku, Y. Iida, E. Sakai, M. Kobayashi, and H. Kumigashira, “Proton conduction of $\text{BaCe}_{0.90}\text{Y}_{0.10}\text{O}_{3-\delta}$ thin film with lattice distortion,” *Solid State Ionics*, vol. 270, pp. 1–5, feb 2015.
- [24] M. Karlsson, M. E. Björketun, P. G. Sundell, A. Matic, G. Wahnström, D. Engberg, L. Börjesson, I. Ahmed, S. Eriksson, and P. Berastegui, “Vibrational properties of protons in hydrated $\text{BaIn}_x\text{Zr}_{1-x}\text{O}_{3-x/2}$,” *Phys. Rev. B*, vol. 72, p. 094303, sep 2005.
- [25] I. Ahmed, S. Eriksson, E. Ahlberg, C. Knee, P. Berastegui, L. Johansson, H. Rundlöf, M. Karlsson, A. Matic, and L. Börjesson, “Synthesis and structural characterization of perovskite type proton conducting $\text{BaZr}_{1-x}\text{In}_x\text{O}_{3-\delta}$ ($0.0 \leq x \leq 0.75$),” *Solid State Ionics*, vol. 177, pp. 1395–1403, jul 2006.
- [26] I. Ahmed, S. Eriksson, E. Ahlberg, C. Knee, M. Karlsson, A. Matic, L. Börjesson, and D. Engberg, “Proton conductivity and low temperature structure of In-doped BaZrO_3 ,” *Solid State Ionics*, vol. 177, pp. 2357–2362, oct 2006.
- [27] M. E. Björketun, P. G. Sundell, and G. Wahnström, “Effect of acceptor dopants on the proton mobility in BaZrO_3 : A density functional investigation,” *Phys. Rev. B*, vol. 76, p. 054307, aug 2007.
- [28] M. Karlsson, A. Matic, S. F. Parker, I. Ahmed, L. Börjesson, and S. Eriksson, “O-H wag vibrations in hydrated $\text{BaIn}_x\text{Zr}_{1-x}\text{O}_{3-x/2}$ investigated with inelastic neutron scattering,” *Phys. Rev. B*, vol. 77, p. 104302, mar 2008.

- [29] M. Karlsson, A. Matic, C. Knee, I. Ahmed, S. Eriksson, and L. Börjesson, "Short-Range Structure of Proton-Conducting Perovskite $\text{BaIn}_x\text{Zr}_{1-x}\text{O}_{3-x/2}$ ($x = 0-0.75$)," *Chem. Mater.*, vol. 20, pp. 3480–3486, may 2008.
- [30] I. Ahmed, C. Knee, M. Karlsson, S. Eriksson, P. F. Henry, A. Matic, D. Engberg, and L. Börjesson, "Location of deuteron sites in the proton conducting perovskite $\text{BaZr}_{0.50}\text{In}_{0.50}\text{O}_{3-y}$," *J. Alloys Compd.*, vol. 450, pp. 103–110, feb 2008.
- [31] F. Giannici, A. Longo, A. Balerna, K. Kreuer, and A. Martorana, "Proton Dynamics in $\text{In}:\text{BaZrO}_3$: Insights on the Atomic and Electronic Structure from X-ray Absorption Spectroscopy," *Chem. Mater.*, vol. 21, pp. 2641–2649, jul 2009.
- [32] M. Karlsson, A. Matic, E. Zanghellini, and I. Ahmed, "Temperature-Dependent Infrared Spectroscopy of Proton-Conducting Hydrated Perovskite $\text{BaIn}_x\text{Zr}_{1-x}\text{O}_{1-x/2}$ ($x = 0.10-0.75$)," *J. Phys. Chem. C*, vol. 114, pp. 6177–6181, apr 2010.
- [33] M. Karlsson, P. Fouquet, I. Ahmed, and M. Maccarini, "Dopant Concentration and Short-Range Structure Dependence of Diffusional Proton Dynamics in Hydrated $\text{BaIn}_x\text{Zr}_{1-x}\text{O}_{3-x/2}$ ($x = 0.10$ and 0.50)," *J. Phys. Chem. C*, vol. 114, pp. 3292–3296, feb 2010.
- [34] D. Zeudmi Sahraoui and T. Mineva, "Effect of dopant nature on structures and lattice dynamics of proton-conducting BaZrO_3 ," *Solid State Ionics*, vol. 253, pp. 195–200, dec 2013.
- [35] E. Kendrick and P. R. Slater, "Battery and solid oxide fuel cell materials," *Annu. Reports Sect. "A" (Inorganic Chem.)*, vol. 109, no. 0, p. 396, 2013.
- [36] N. Mahato, A. Banerjee, A. Gupta, S. Omar, and K. Balani, "Progress in material selection for solid oxide fuel cell technology: A review," *Prog. Mater. Sci.*, vol. 72, pp. 141–337, 2015.
- [37] L. Bi, S. Boulfrad, and E. Traversa, "Steam electrolysis by solid oxide electrolysis cells (SOECs) with proton-conducting oxides," *Chem. Soc. Rev.*, vol. 43, pp. 8255–8270, aug 2014.
- [38] H. Iwahara, T. Esaka, H. Uchida, and N. Maeda, "Proton conduction in sintered oxides and its application to steam electrolysis for hydrogen production," *Solid State Ionics*, vol. 3-4, pp. 359–363, aug 1981.

- [39] H. Iwahara, H. Uchida, and S. Tanaka, “High temperature type proton conductor based on SrCeO_3 and its application to solid electrolyte fuel cells,” *Solid State Ionics*, vol. 9-10, pp. 1021–1025, dec 1983.
- [40] H. Iwahara, T. Esaka, H. Uchida, T. Yamauchi, and K. Ogaki, “High temperature type protonic conductor based on SrCeO_3 and its application to the extraction of hydrogen gas,” *Solid State Ionics*, vol. 18-19, pp. 1003–1007, jan 1986.
- [41] H. Iwahara, “Proton Conduction in Sintered Oxides Based on BaCeO_3 ,” *J. Electrochem. Soc.*, vol. 135, p. 529, feb 1988.
- [42] K. Kreuer, “Aspects of the formation and mobility of protonic charge carriers and the stability of perovskite-type oxides,” *Solid State Ionics*, vol. 125, pp. 285–302, oct 1999.
- [43] P. T. N. Kochetova, I. Animitsa, D. Medvedev, A. Demin, “Recent activity in the development of proton-conducting oxides for high-temperature applications,” *RSC Adv.*, vol. 6, no. 77, pp. 73222–73268, 2016.
- [44] V. M. Goldschmidt, “Die Gesetze der Krystallochemie,” *Naturwissenschaften*, vol. 14, pp. 477–485, may 1926.
- [45] C. Moure and O. Peña, “Recent advances in perovskites: Processing and properties,” *Prog. Solid State Chem.*, vol. 43, no. 4, pp. 123–148, 2015.
- [46] F. Giannici, M. Shirpour, A. Longo, A. Martorana, R. Merkle, and J. Maier, “Long-Range and Short-Range Structure of Proton-Conducting Y:BaZrO_3 ,” *Chem. Mater.*, vol. 23, pp. 2994–3002, jun 2011.
- [47] A. R. Akbarzadeh, I. Kornev, C. Malibert, L. Bellaiche, and J. M. Kiat, “Combined theoretical and experimental study of the low-temperature properties of BaZrO_3 ,” *Phys. Rev. B*, vol. 72, p. 205104, nov 2005.
- [48] A. I. Lebedev and I. A. Sluchinskaya, “Structural instability in BaZrO_3 crystals: Calculations and experiment,” *Phys. Solid State*, vol. 55, pp. 1941–1945, sep 2013.
- [49] A. I. Lebedev and I. A. Sluchinskaya, “Combined first-principles and EXAFS study of structural instability in BaZrO_3 ,” *J. Adv. Dielectr.*, vol. 05, p. 1550019, sep 2015.

- [50] T. S. Bjørheim, E. A. Kotomin, and J. Maier, “Hydration entropy of BaZrO₃ from first principles phonon calculations,” *J. Mater. Chem. A*, vol. 3, pp. 7639–7648, mar 2015.
- [51] T. Norby, M. Wideroe, R. Glockner, and Y. Larring, “Hydrogen in oxides.,” *Dalton Trans.*, pp. 3012–8, oct 2004.
- [52] K. Kreuer, “On the development of proton conducting materials for technological applications,” *Solid State Ionics*, vol. 97, pp. 1–15, may 1997.
- [53] I. Ahmed, S. Eriksson, E. Ahlberg, C. Knee, L. Johansson, M. Karlsson, A. Matic, L. Börjesson, and H. Götlind, “Structural study and proton conductivity in Yb-doped BaZrO₃,” *Solid State Ionics*, vol. 178, pp. 515–520, apr 2007.
- [54] I. Ahmed, M. Karlsson, S. Eriksson, E. Ahlberg, C. Knee, K. Larsson, A. K. Azad, A. Matic, and L. Börjesson, “Crystal Structure and Proton Conductivity of BaZr_{0.9}Sc_{0.1}O_{3-δ},” *J. Am. Ceram. Soc.*, vol. 91, pp. 3039–3044, sep 2008.
- [55] E. Fabbri, D. Pergolesi, S. Licocchia, and E. Traversa, “Does the increase in Y-dopant concentration improve the proton conductivity of BaZr_{1-x}Y_xO_{3-δ} fuel cell electrolytes?,” *Solid State Ionics*, vol. 181, pp. 1043–1051, jul 2010.
- [56] M. E. Björketun, P. G. Sundell, and G. Wahnström, “Structure and thermodynamic stability of hydrogen interstitials in BaZrO₃ perovskite oxide from density functional calculations,” *Faraday Discuss.*, vol. 134, pp. 247–265, dec 2007.
- [57] E. J. Spahr, L. Wen, M. Stavola, L. Boatner, L. C. Feldman, N. H. Tolk, and G. Lüpke, “Proton Tunneling: A Decay Channel of the O-H Stretch Mode in KTaO₃,” *Phys. Rev. Lett.*, vol. 102, p. 075506, feb 2009.
- [58] E. J. Spahr, L. Wen, M. Stavola, L. Boatner, L. C. Feldman, N. H. Tolk, and G. Lüpke, “Giant Enhancement of Hydrogen Transport in Rutile TiO₂ at Low Temperatures,” *Phys. Rev. Lett.*, vol. 104, p. 205901, may 2010.
- [59] M. Glerup, “Vibrational spectroscopy on protons and deuterons in proton conducting perovskites,” *Solid State Ionics*, vol. 148, pp. 83–92, may 2002.

- [60] Y. Yamazaki, F. Blanc, Y. Okuyama, L. Buannic, J. C. Lucio-Vega, C. P. Grey, and S. M. Haile, “Proton trapping in yttrium-doped barium zirconate,” *Nat. Mater.*, vol. 12, pp. 647–51, jul 2013.
- [61] E. Jedvik, A. Lindman, M. . Benediktsson, and G. Wahnström, “Size and shape of oxygen vacancies and protons in acceptor-doped barium zirconate,” *Solid State Ionics*, vol. 275, pp. 2–8, 2015.
- [62] R. Steudel, “Infrared and Raman Spectroscopy. Methods and Applications. Edited by Bernhard Schrader, VCH, Weinheim 1995, XVIII, 787 pp., hardcover, DM 298.00, ISBN 3-527-26446-9,” *Adv. Mater.*, vol. 9, pp. 275–276, mar 1997.
- [63] N. B. Colthup, L. H. Daly, and S. E. Wiberley, *Introduction to Infrared and Raman Spectroscopy*. Elsevier, 1990.
- [64] P. Larkin, *Infrared and Raman Spectroscopy*. Elsevier, 2011.
- [65] P. C. H. Mitchell, S. F. Parker, A. Ramirez-Cuesta, and J. Tomkinson, *Vibrational Spectroscopy with Neutrons*. Singapore: World Scientific, 2005.
- [66] G. Squires, *Introduction to the Theory of Thermal Neutron Scattering*. Dover Publications, 1978.
- [67] S. Lovesey, *Theory of neutron scattering from condensed matter*. 1984.
- [68] J. Tomkinson, M. Warner, and A. Taylor, “Powder averages for neutron spectroscopy of anisotropic molecular oscillators,” *Mol. Phys.*, vol. 51, pp. 381–392, aug 2006.
- [69] S. F. Parker, S. M. Bennington, A. J. Ramirez-Cuesta, G. Auffermann, W. Bronger, H. Herman, K. P. J. Williams, and T. Smith, “Inelastic neutron scattering and Raman spectroscopies and periodic DFT studies of Rb_2PtH_6 and Rb_2PtD_6 ,” *J. Am. Chem. Soc.*, vol. 125, pp. 11656–61, sep 2003.
- [70] J. Tomkinson, S. F. Parker, and D. Lennon, “No evidence for Evans’ holes in the A, B, C vibrational structure of potassium dihydrogen arsenate,” *J. Chem. Phys.*, vol. 133, p. 034508, jul 2010.
- [71] T. Sander, C. T. Reindl, M. Giar, B. Eifert, M. Heinemann, C. Heiliger, and P. J. Klar, “Correlation of intrinsic point defects and the Raman modes of cuprous oxide,” *Phys. Rev. B*, vol. 90, p. 045203, jul 2014.

- [72] J. Daillant and A. Gubaud, *X-ray and Neutron Reflectivity*, vol. 770 of *Lecture Notes in Physics*. Berlin, Heidelberg: Springer Berlin Heidelberg, 2009.
- [73] L. Parratt, “Surface Studies of Solids by Total Reflection of X-Rays,” *Phys. Rev.*, vol. 95, pp. 359–369, jul 1954.
- [74] M. Björck and G. Andersson, “GenX: an extensible X-ray reflectivity refinement program utilizing differential evolution,” *J. Appl. Crystallogr.*, vol. 40, pp. 1174–1178, nov 2007.
- [75] M. Wilde and K. Fukutani, “Hydrogen detection near surfaces and shallow interfaces with resonant nuclear reaction analysis,” *Surf. Sci. Rep.*, vol. 69, pp. 196–295, dec 2014.
- [76] G. Shirane, S. M. Shapiro, and John M. T., *Neutron Scattering with a Triple-Axis Spectrometer*. Cambridge: Cambridge University Press, 1st ed., 2002.
- [77] R. Bewley, R. Eccleston, K. McEwen, S. Hayden, M. Dove, S. M. Bennington, J. Treadgold, and R. Coleman, “MERLIN, a new high count rate spectrometer at ISIS,” *Phys. B Condens. Matter*, vol. 385-386, pp. 1029–1031, nov 2006.
- [78] S. F. Parker, F. Fernandez-Alonso, A. J. Ramirez-Cuesta, J. Tomkinson, S. Rudic, R. S. Pinna, G. Gorini, and J. Fernández Castañón, “Recent and future developments on TOSCA at ISIS,” *J. Phys. Conf. Ser.*, vol. 554, p. 012003, nov 2014.
- [79] “<http://www.isis.stfc.ac.uk/index.html>.”
- [80] W. Herres and J. Gronholz, “Understanding FT-IR Data Processing,” *J. Comput. Appl. Lab.*, vol. 2, pp. 216–220, 1984.
- [81] “NCNR(NIST): <https://www.ncnr.nist.gov/>.”
- [82] J. A. Dura, D. J. Pierce, C. F. Majkrzak, N. C. Maliszewskyj, D. J. McGillivray, M. Lösche, K. V. O’Donovan, M. Mihailescu, U. Perez-Salas, D. L. Worcester, and S. H. White, “AND/R: Advanced neutron diffractometer/reflectometer for investigation of thin films and multilayers for the life sciences,” *Rev. Sci. Instrum.*, vol. 77, pp. 74301–7430111, jul 2006.

- [83] “ILL: <https://www.ill.eu/>.”
- [84] R. Cubitt and G. Fragneto, “D17: the new reflectometer at the ILL,” *Appl. Phys. A Mater. Sci. Process.*, vol. 74, pp. s329–s331, dec 2002.

